

Influence of Leading Design Parameters on the Force Performance of a Complementary and Modular Linear Flux-Switching Permanent-Magnet Motor

Ruiwu Cao, *Student Member, IEEE*, Ming Cheng, *Senior Member, IEEE*,
Chunting Chris Mi, *Fellow, IEEE*, and Wei Hua, *Member, IEEE*

Abstract—This paper investigates the influence of some leading design parameters on the force performance of a new complementary and modular linear flux-switching permanent-magnet (LFSPM) motor. The originality of the proposed structure is that each phase consists of two “E”-shaped modules, whose positions are mutually 180° electrical degrees apart. Also, there is a flux barrier between the two modules. First, the structure and influence of some leading design parameters on the force performance of the complementary and modular LFSPM motor are analyzed. Then, a conventional LFSPM motor obtained directly from a rotary FSPM motor is optimized and compared with the complementary and modular LFSPM motor based on finite-element method. The results reveal that the proposed motor has sinusoidal and symmetrical three-phase back electromotive force waveforms and smaller cogging force and force ripple than the existing motors. Moreover, a prototype of the proposed motor is built to validate the study.

Index Terms—Cogging force, complementary and modular, linear flux-switching permanent-magnet (LFSPM) motor, linear motor, speed control.

NOMENCLATURE

F_{avg}	Average thrust force.
F_{ripple}	Thrust force ripple.
F_{cog}	Cogging force ripple.
F_{x_AA}	Cogging force of phase A.
F_{x_BB}	Cogging force of phase B.
F_{x_CC}	Cogging force of phase C.
F_x	Sum of F_{x_AA} , F_{x_BB} , and F_{x_CC} .
F_{x_AABBCC}	Total cogging force.
F_{y_AA}	Normal force of phase A.
F_{y_BB}	Normal force of phase B.
F_{y_CC}	Normal force of phase C.
F_y	Sum of F_{y_AA} , F_{y_BB} , and F_{y_CC} .
F_{y_AABBCC}	Total normal force.

Manuscript received March 20, 2013; revised May 23, 2013; accepted May 28, 2013. Date of publication June 28, 2013; date of current version October 18, 2013. This work was supported by the 973 Program of China under Project 2013CB035603 and the Scientific Research Foundation of Graduate School of Southeast University (YBPY1201).

R. Cao, M. Cheng, and W. Hua are with the School of Electrical Engineering, Southeast University, Nanjing 210096, China (e-mail: ruiwucao@gmail.com; mcheng@seu.edu.cn; huawei1978@seu.edu.cn).

C. C. Mi is with the College of Engineering and Computer Science, University of Michigan, Dearborn, MI 48128 USA (e-mail: chrismi@umich.edu).

Color versions of one or more of the figures in this paper are available online at <http://ieeexplore.ieee.org>.

Digital Object Identifier 10.1109/TIE.2013.2271603

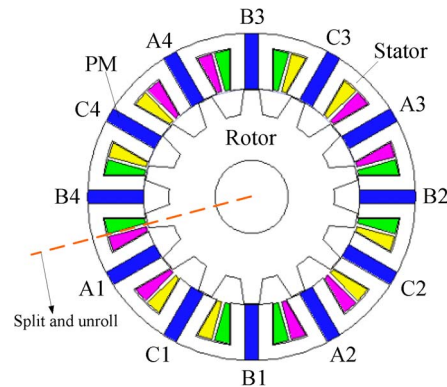


Fig. 1. Cross section of the 12/14-pole LFSPM motor.

h_{pm}	PM high.
h_{st}	Stator tooth high.
h_s	Stator high.
k_{st}	Coefficient of stator tooth width.
k_{sy}	Coefficient of stator tooth yoke width.
k_{my}	Coefficient of mover yoke high.
k_{sty}	Coefficient of stator tooth yoke width.
N_{coil}	Number of coils per “E”-shaped module.
w_{ms}	Slot width.
τ_m	Mover pole pitch.
λ_1	Relative position of the two “E”-shaped modules in one phase.
λ_2	Relative displacement between the modules of the adjacent two phases.

I. INTRODUCTION

LINEAR motors produce a direct thrust force without the need of conversion from rotational torque to linear force. Therefore, they are ideal for rail transportation systems [1]–[3]. The conventional linear permanent-magnet synchronous (LPMS) motor exhibits higher efficiency and higher power density than linear induction motors [4]. However, in applications with a long stator, such as in urban rail systems, the conventional LPMS motor inevitably results in significant cost increase due to a large amount of magnets or armature windings set along the long stator. Linear switched reluctance (LSR) motors have a simpler and more rugged structure, and a lower system cost than direct-drive LPMS motor due to its simple stator, which only consists of iron [5]. However, this motor also

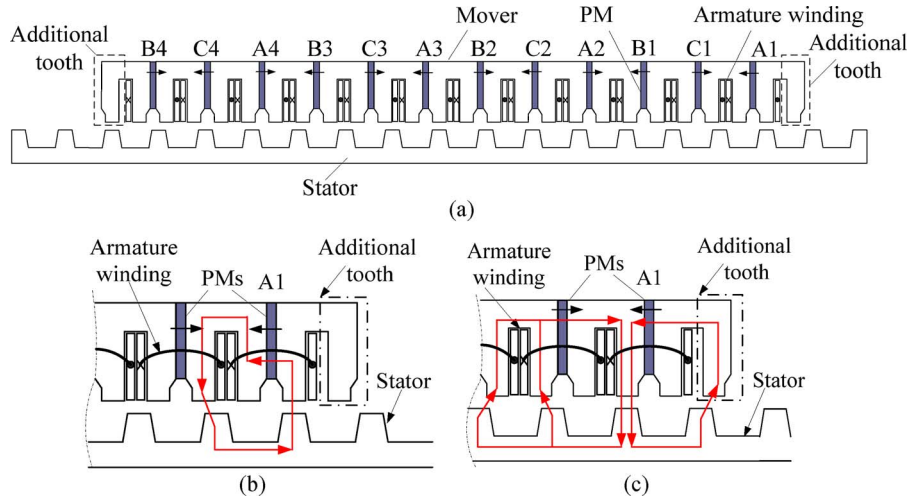


Fig. 2. Cross section of the conventional LFSPM motor and its unbalanced magnetic circuit principle. (a) Cross section of the conventional LFSPM motor. (b) Mover position with the positive maximum flux linkage in coil A1. (c) Mover position with the negative maximum flux linkage in coil A1.

suffers from drawbacks such as higher torque ripples and lower power density than the permanent-magnet (PM) motors as in the rotary structure [6]. Hence, how to incorporate the merits of both higher power density and simpler lower cost long stator has attracted more and more attention.

In recent years, new kinds of primary PM linear motors [7]–[10], namely, the linear structure of stator-PM motors [11]—doubly salient PM (DSPM) motors, flux reversal PM motors, and flux-switching PM (FSPM) motors—have attracted attention, in which both the PMs and the armature windings are placed in the same short primary mover, while the long secondary stator is only made of iron. Hence, this kind of linear PM motor incorporates the merits of the simple structure of linear induction motors and LSR motors, and the high power density of LPMS motors, which are perfectly suited for long stator application.

It has been shown that the FSPM motor can offer high power density [12], sinusoidal back electromotive force (EMF), and fault-tolerance capabilities [13], as compared with the DSPM motor. Therefore, the linear structure of FSPM motor will be investigated in this paper. Fig. 1 shows a rotary 12/14-pole FSPM motor. Its operation principle and electromagnetic performance were investigated and compared with a 12/10-pole FSPM motor in [14]. The results show that its output torque is much higher and its torque ripple is much smaller than that of the 12/10-pole FSPM motor. Hence, the linear FSPM (LFSPM) motors based on the 12/14-pole rotary FSPM motor will be investigated in this paper. Fig. 2(a) shows an LFSPM motor, which can be obtained by splitting the rotary 12/14-pole FSPM motor (as shown in Fig. 1) along the radial direction and unrolling it. Also, in order to balance the magnetic circuit of the end coil, two additional teeth are added at each end of the primary mover. For comparison, this motor is named conventional LFSPM motor in this paper. Obviously, the basic operation principle of the conventional LFSPM motor is the same as the rotary FSPM motor. However, this LFSPM motor suffers from some drawbacks such as unbalanced magnetic circuit for the end coils, bigger cogging force, and thrust force ripple. To analyze the principle of unbalance magnetic circuit of the end coils, the

magnetic circuit of end coil A1 at two positions is shown in Fig. 2(b) and (c), where the flux linkage in coil A1 reaches the positive maximum and negative minimum values, respectively. It can be seen that the flux linkage in coil A1 is excited by one PM at the position shown in Fig. 2(b) and by two PMs at the position shown in Fig. 2(c), which will lead to the unbalanced magnetic circuit of the end coils in one electrical period.

In order to solve the problems in the conventional LFSPM motor, namely, unbalanced magnetic circuit and big cogging force, a new complementary and modular LFSPM (CMLFSPM) motor has been proposed in [15] and [16]. However, this paper mainly focused on the operation principle and mathematics model of the CMLFSPM motor. It has been identified that the rotor pole-arc affects not only the shape of back EMF but also the cogging torque of the rotary FSPM motor [17]. Also, the leading parameters have a significant influence on the electromagnetic performance of a linear PM motor [18]. Therefore, the purpose of this paper is to investigate the influences of some key design parameters on the electromagnetic performance of the CMLFSPM motor so as to lay a foundation for design optimization of the motor. Furthermore, the dynamic performances of the closed-loop speed control of LFSPM motor are investigated for the first time.

The rest of this paper is organized as follows. The basic structure of the CMLFSPM motor is explained in Section II. In Section III, the influences of some key parameters on the average thrust force, force ripple, and cogging force of the proposed motor are investigated. In Section IV, the electromagnetic performance and cogging force of the optimized CMLFSPM motor are described in detail. In Section V, the back EMF, cogging force, and dynamic performances of the prototype CMLFSPM motor are evaluated based on experiments. Finally, the conclusion is drawn in Section VI.

II. OPERATION PRINCIPLE AND STRUCTURE

Fig. 3 shows the cross section of the CMLFSPM motor. It can be seen that each phase consists of two “E”-shaped modules

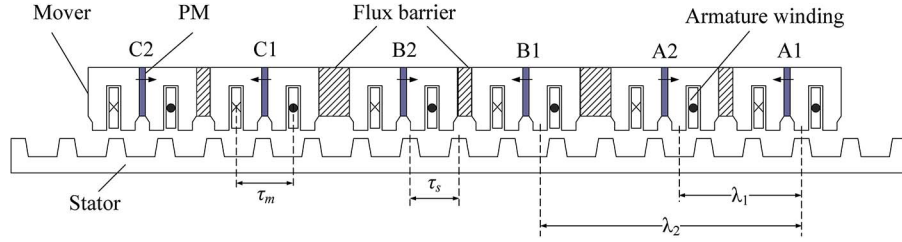


Fig. 3. Cross section of the CMLFSPM motor, $\lambda_1 = (2 + 1/2)\tau_s$ and $\lambda_2 = (5 + 1/3)\tau_s$.

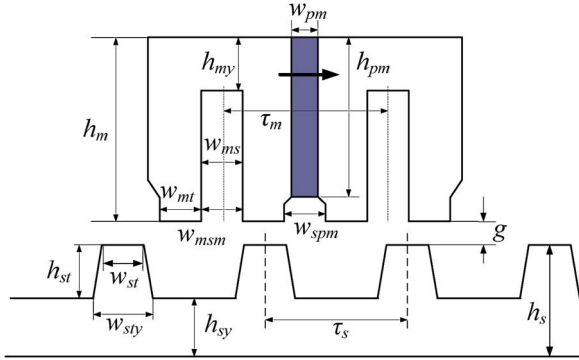


Fig. 4. Design parameters of the "E"-shaped module and stator.

whose positions are mutually λ_1 apart

$$\lambda_1 = (k + 1/2)\tau_s \quad (1)$$

where τ_s is the stator pole pitch and k is a positive integer ($k = 2$). Each "E"-shaped module consists of two pieces of "U"-shaped iron, between which a PM is sandwiched. The armature winding coils are located in the slot and wound around the adjacent teeth of the two "U"-shaped modules. The two coils of phase A, namely, coil A1 and coil A2, are connected in series. The two PMs in the two "E"-shaped modules are magnetized in opposite directions. The structure of phase B and phase C is the same as that of phase A.

For a three-phase motor, the relative displacement between the modules of the adjacent two phases is equal to

$$\lambda_2 = (j \pm 1/3)\tau_s \text{ or } \lambda_2 = (j \pm 1/6)\tau_s \quad (2)$$

where j is a positive integer ($j = 5$). There is a flux barrier between every two adjacent "E"-shaped modules. When the mover moves by one stator pole pitch, the phase flux linkage and back EMF waveforms are bipolar, sinusoidal, complementary, and symmetrical.

To investigate the influence of the leading parameters on the force performance of the CMLFSPM motor, some key parameters are defined in Fig. 4, and the detailed original parameters are listed in Table I. Also, it is necessary to explain the original value of some key parameters and to define some coefficients.

1) Different from the rotary FSPM motor, the PMs are designed a little shorter than the mover teeth. The mover tooth width w_{mt} , the slot open width w_{msm} , and the width of the slot under PM w_{spm} satisfy the relationship $w_{mt} = w_{msm} = w_{spm} = \tau_m/4$ as shown in Fig. 4.

TABLE I
DESIGN SPECIFICATIONS OF CMLFSPM MOTOR

Items	Original parameters
Rated speed, v (m/s)	1.5
Mover stack length, l_m (mm)	120
Mover pole pitch, τ_m (mm)	42
Stator pole pitch, τ_s (mm)	$\tau_m * 12/14$
Mover tooth width, w_{mt} (mm)	$\tau_m/4$
Mover slot open width, w_{msm} (mm)	$\tau_m/4$
Mover slot width, w_{ms} (mm)	$\tau_m/4$
Slot width (under PM), w_{spm} (mm)	$\tau_m/4$
Mover height, h_m (mm)	50
Mover yoke height, h_{my} (mm)	$0.75 * \tau_m/2$
Magnet height, h_{pm} (mm)	$0.9 * h_m$
Magnet width, w_{pm} (mm)	$\tau_m/4$
Air gap length, g (mm)	1
Stator tooth width, w_{st} (mm)	$1.5 * \tau_m/4$
Stator teeth yoke width, w_{sty} (mm)	$1.5 * \tau_m/4$
Stator tooth height, h_{st} (mm)	15
Stator yoke height, h_{sy} (mm)	20
Copper filling factor	0.4
Stator height, h_s (mm)	35
Number of turns per coil, N_{coil}	116
Stack factor	0.95
Current density J_s (A/mm ²)	5.85

- 2) The original value of PM width w_{pm} is designed to be the same as the mover teeth, i.e., $w_{mt} = w_{pm} = \tau_m/4$.
- 3) The original values of mover yoke height h_{my} , stator tooth width w_{st} , stator tooth yoke width w_{sty} , and stator yoke height h_{sy} are designed to be bigger than the mover tooth.
- 4) The mover height h_m , the motor stack length l_m , and air gap length g are kept constant.
- 5) In order to optimize w_{st} , w_{pm} , h_{my} , h_{pm} , h_{st} , h_{sy} , and w_{sty} , some coefficients are defined as

$$k_{st} = \frac{w_{st}}{\tau_m/4} \quad (3)$$

$$k_{my} = \frac{h_{my}}{\tau_m/2} \quad (4)$$

$$k_{sty} = \frac{w_{sty}}{\tau_m/4} \quad (5)$$

- 6) k_{pm_L} and k_{pm_w} are the ratios of the changed PM length and width to the original one, respectively. k_{hst} and k_{hsy} are the ratios of the changed stator tooth height and stator yoke height to the original value, respectively.

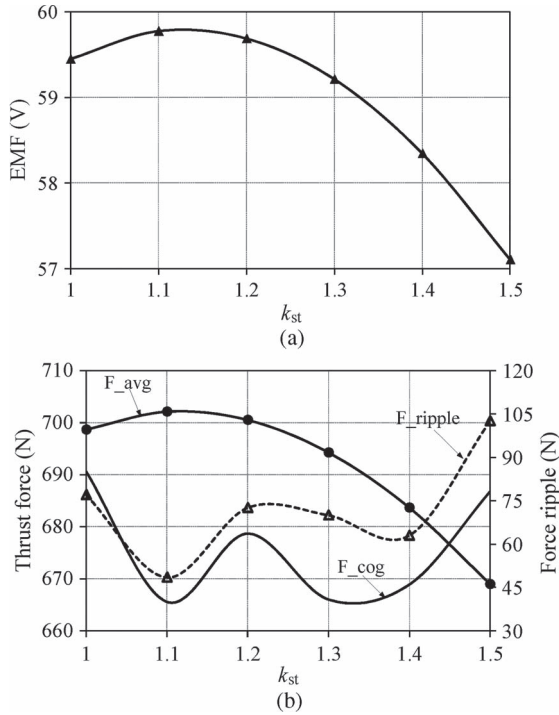


Fig. 5. Back EMF and force performances of the CMLFSPM motor versus k_{st} . (a) Back EMF. (b) Thrust force, force ripple, and cogging force.

III. STUDY OF THE INFLUENCE OF SOME LEADING PARAMETERS ON FORCE PERFORMANCE OF BOTH MOTORS

A. Influence of k_{st} and Magnet Dimensions

In this paper, the transient solver of Ansys Maxwell-2D software is used to solve the electromagnetic characteristic of the two LFSPM motors. Because the cogging torque of the rotary FSPM motor is sensitive to the rotor tooth width [19], the influence of the coefficient k_{st} on the performance of the CMLFSPM motor will be investigated by means of the finite-element method (FEM) first.

Fig. 5(a) shows the rms value of the back EMF of the CMLFSPM motor at the rated speed (1.5 m/s) for k_{st} in the range of 1–1.5 while keeping other parameters constant. It can be seen that, when k_{st} is about 1.1, the back EMF reaches the maximum value. Also, the peak-to-peak values of the cogging force F_{cog} , average thrust force F_{avg} , and thrust force ripple F_{ripple} at the rated current density are calculated by means of FEM as shown in Fig. 5(b). Obviously, F_{avg} reaches the maximum value, and F_{ripple} and F_{cog} all reach the minimum value at $k_{st} = 1.1$. The detailed values of the back EMF, F_{avg} , F_{ripple} , and F_{cog} at different k_{st} values are listed in Table II. Hence, in this stage, $k_{st} = 1.1$ is adopted.

As aforementioned, the original PM width is the same as a quarter of the mover pole pitch ($\tau_m/4$). In fact, the PM dimensions should be optimized according to the actual requirement. There are two methods used in reducing the PM height, namely, reducing the PM height from top to bottom or from bottom to top. The current research shows that reducing the PM height of the FSPM motor from the top can offer higher force ability by using the same PMs [19]. Hence, this method

TABLE II
ELECTROMAGNETIC PERFORMANCES OF CMLFSPM MOTOR AS A FUNCTION OF k_{st}

k_{st}	EMF (V)	F_{cog} (N)	F_{avg} (N)	F_{ripple} (N)
1	59.45	85.28	698.66	77.08
1.1	59.78	39.98	702.13	48.47
1.2	59.69	63.65	700.53	72.59
1.3	59.21	40.79	694.26	69.99
1.4	58.35	45.96	683.66	63
1.5	57.1	78.27	668.96	102.64

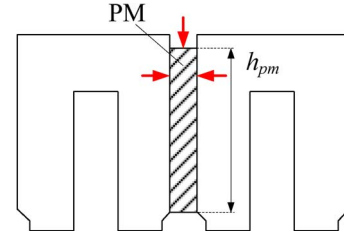


Fig. 6. Schematic of PM optimization.

TABLE III
AVERAGE THRUST FORCE FOR DIFFERENT MAGNET DIMENSIONS

k_{pm_L}	k_{pm_W}				
	1	0.9	0.8	0.7	0.6
1	702.13	727.06	736.36	729.53	705.69
0.9	703.72	721.87	724.25	711.53	683.4
0.8	698.75	709.95	706.59	689.25	657.63
0.7	685.78	691.02	683.02	662.37	628.74

is also adopted in the CMLFSPM motor, as shown in Fig. 6. Based on this method, PM dimensions are calculated by using FEM. The average thrust force values at a given current density and at original parameters when k_{pm_L} is in the range of 1–0.7 and k_{pm_w} is in the range of 1–0.6 are listed in Table III. It can be seen from Table III that the PM utilization ratio when $k_{pm_L} = 1$ and k_{pm_w} is in the range of 1–0.6 is bigger than that when $k_{pm_w} = 1$ and k_{pm_w} is in the range of 1–0.7. Also, F_{avg} reaches the maximum value when $k_{pm_w} = 0.8$ and $k_{pm_L} = 1$, which is about 104.9% of the one with the original PM dimensions but using 80% PM volume. Moreover, F_{avg} at $k_{pm_w} = 0.7$ and $k_{pm_L} = 1$ is about 99.1% of the one at $k_{pm_w} = 0.8$ and $k_{pm_L} = 1$. Hence, to save the expensive PM material, $k_{pm_w} = 0.7$ and $k_{pm_L} = 1$ are adopted for the next step work.

B. Influence of Mover Yoke Height

Since the original mover yoke height of the CMLFSPM motor is chosen big enough to avoid magnetic saturation, coefficient k_{my} will be optimized in the range of 0.75–0.55. Meanwhile, the coil number and the applied current density are kept constant, which means that the applied phase current and copper loss will increase with the reduction of h_{my} . The electromagnetic performances of the CMLFSPM motor including the back EMF, F_{avg} , F_{ripple} , F_{cog} , and the average thrust force per unit copper loss F_{avg}/P_{cu} are calculated as shown

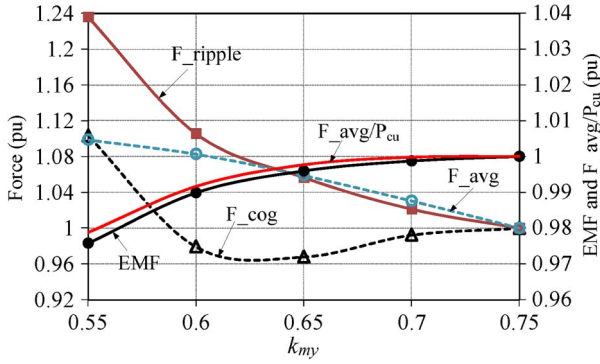


Fig. 7. Back EMF and force performance of the CMLFSPM motor versus k_{my} .

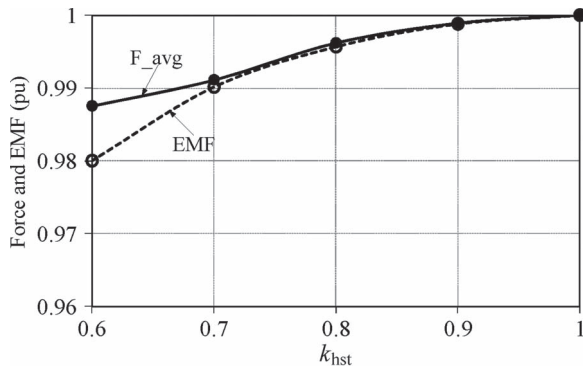


Fig. 8. Back EMF and average thrust force of the CMLFSPM motor versus k_{hst} .

in Fig. 7. It can be seen that F_{avg} and F_{ripple} vary inversely with coefficient k_{my} . When k_{my} is smaller than 0.65, the back EMF decreases obviously with k_{my} , which is caused by the mover yoke saturation due to the decrease of mover yoke width. Also, F_{avg}/P_{cu} decreases with k_{my} obviously when k_{my} is smaller than 0.65. Moreover, the cogging force ripple also reaches around the minimum value at $k_{my} = 0.65$. Therefore, by considering the saturation, copper loss, and cogging force, $k_{my} = 0.65$ is chosen for the next step work.

C. Influence of Stator Tooth and Yoke Height

The original dimensions of stator tooth and yoke of the CMLFSPM motor are chosen to avoid the magnetic flux leakage and magnetic saturation. To save the stator material, the influence of coefficients k_{hst} and k_{hsy} will be discussed in this section. Fig. 8 shows the back EMF and F_{avg} when k_{hst} is in the range of 1–0.6, i.e., h_{st} is in the range of 15–9 mm. It can be seen that, when k_{hst} is smaller than 0.9, the coefficient of magnetic flux leakage increases. In theory, $k_{hst} = 0.6$ is acceptable because the rms value of the back EMF is about 0.98 and F_{avg} is about 0.988 of the original dimension. However, to reduce the effect of magnetic flux leakage in the prototype motor, $k_{hst} = 0.8$ is adopted in this paper.

Fig. 9 shows F_{avg} , F_{ripple} , F_{cog} , and rms value of the back EMF of the CMLFSPM motor when k_{hsy} is in the range of 1–0.5, i.e., h_{sy} is in the range of 20–10 mm. It can be seen that, when k_{hsy} is smaller than 0.75, the back EMF and average

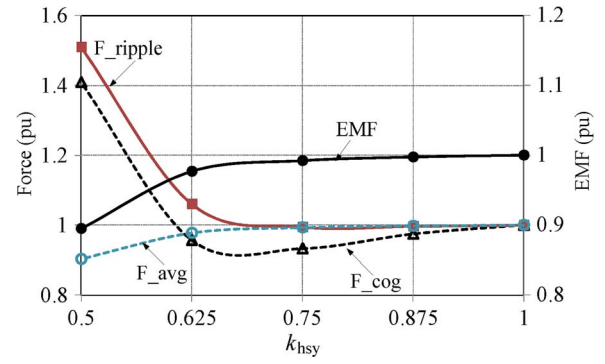


Fig. 9. Back EMF and force performance of the CMLFSPM motor versus k_{hsy} .

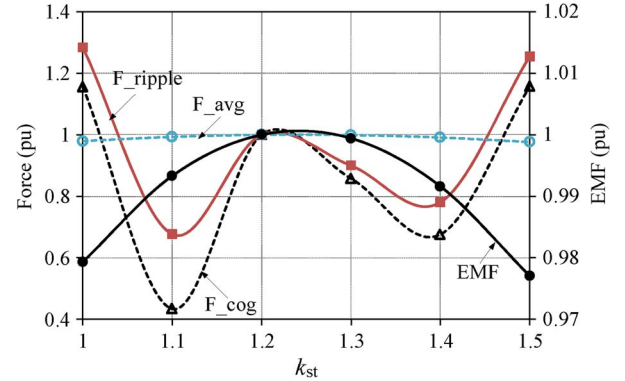


Fig. 10. Back EMF and force performance of the CMLFSPM motor versus k_{st} .

thrust force decrease, while F_{ripple} and F_{cog} vary inversely with coefficient k_{hsy} . Also, F_{ripple} and F_{cog} are around the minimum value when $k_{hsy} = 0.75$. Hence, $k_{hst} = 0.8$ and $k_{hsy} = 0.75$ are chosen for the next step work.

D. Influence of k_{st}

Since the cogging force of the CMLFSPM motor is sensitive to coefficient k_{st} , in this section, the influence of k_{st} will be analyzed again. Fig. 10 shows F_{avg} , rms value of the back EMF, F_{ripple} , and F_{cog} waveforms of the CMLFSPM motor versus k_{st} . It can be seen that, when $k_{st} = 1.1$, F_{cog} and F_{ripple} reach the minimum value, while F_{avg} and back EMF are about 99.35% and 99.34% of the maximum value at $k_{st} = 1.2$, respectively. Also, the detailed values of the back EMF, F_{avg} , F_{ripple} , and F_{cog} at different k_{st} values are listed in Table IV. Hence, $k_{st} = 1.1$ is chosen to be the optimal dimension for the CMLFSPM motor in this paper. Up to now, the influences of some key parameters of the CMLFSPM motor have been analyzed. The optimal dimensions of the CMLFSPM motor are compared with the original one in Table V. Obviously, the cogging force, thrust force ripple, and PM volume of the optimized structure are about 36.8%, 49.9%, and 70% of those of the original one, while the average thrust force and rms value of the back EMF are about 114.1% and 108% of the original ones, respectively. Also, the stator volume is reduced.

TABLE IV
ELECTROMAGNETIC PERFORMANCES OF CMLFSPM
MOTOR AT DIFFERENT k_{st} VALUES

k_{st}	EMF (V)	F_{cog} (N)	F_{avg} (N)	F_{ripple} (N)
1	60.8	76.75	752.72	97.18
1.04	61.2	55.92	757.63	78.89
1.07	61.46	37.39	760.67	61.63
1.1	61.67	28.83	763.21	51.25
1.13	61.84	43.95	765.33	59.14
1.16	61.98	57.98	766.87	68.37
1.2	62.09	66.41	768.22	75.71
1.3	62.05	56.99	767.6	68.14
1.4	61.57	44.9	761.51	59.1

TABLE V
OPTIMIZED DIMENSION OF CMLFSPM MOTOR

Items	Initial	Optimized
h_{my} (mm)	$0.75 * \tau_m / 2$	$0.65 * \tau_m / 2$
w_{pm} (mm)	$\tau_m / 4$	$0.7 * \tau_m / 4$
w_{st} (mm)	$1.5 * \tau_m / 4$	$1.1 * \tau_m / 4$
h_{st} (mm)	15	12
h_{sy} (mm)	20	15
EMF (V)	57.1	61.67
F_{avg} (N)	668.96	763.21
F_{cog} (N)	78.27	28.83
F_{ripple} (N)	102.64	51.25

E. Influence of k_{st} and Magnet Dimensions on Conventional LFSPM Motor

As can be seen from Figs. 2(a) and 3, the mover of both motors consists of “U”-shaped iron, PMs, and armature windings. If the dimensions of the “U”-shaped iron and the PM of both motors are the same, the total PM volume of the conventional LFSPM motor is twice as much as the CMLFSPM motor, which will lead to high magnetic saturation in the “U”-shaped iron of the conventional LFSPM motor. For fair comparison, the PM width of the conventional LFSPM motor should be optimized, and other key parameters are kept constant. Also, to obtain a smaller cogging force, coefficient k_{st} is optimized in the range of 1–1.5. In this section, the conventional LFSPM motor is optimized through the following three steps.

- 1) F_{avg} , F_{cog} , and F_{ripple} of the conventional LFSPM motor versus k_{st} are shown in Fig. 11(a) when the dimensions of the “U”-shaped iron and the PM are the same as the optimized CMLFSPM motor. Obviously, F_{cog} and F_{ripple} reach the minimum value at $k_{st} = 1.1$, while F_{avg} is about 99.5% of the maximum at $k_{st} = 1.2$. Hence, $k_{st} = 1.1$ is adopted for the next step work to optimize PM width.
- 2) The waveforms of F_{avg} , F_{cog} , and F_{ripple} of the conventional LFSPM motor versus k_{pm-w} are shown in Fig. 11(b). It can be seen that, when $k_{pm-w} = 0.6$, F_{avg} , F_{cog} , and F_{ripple} all reach the maximum value. F_{avg} is about 119% of the optimized CMLFSPM motor, while the total PM volume is about 171% of the CMLFSPM motor. If the total PMs of both motors are the same, i.e., when k_{pm-w} of the conventional LFSPM motor is equal to 0.35, F_{avg} is about 102% of the optimized CMLFSPM motor. Hence, considering the PM

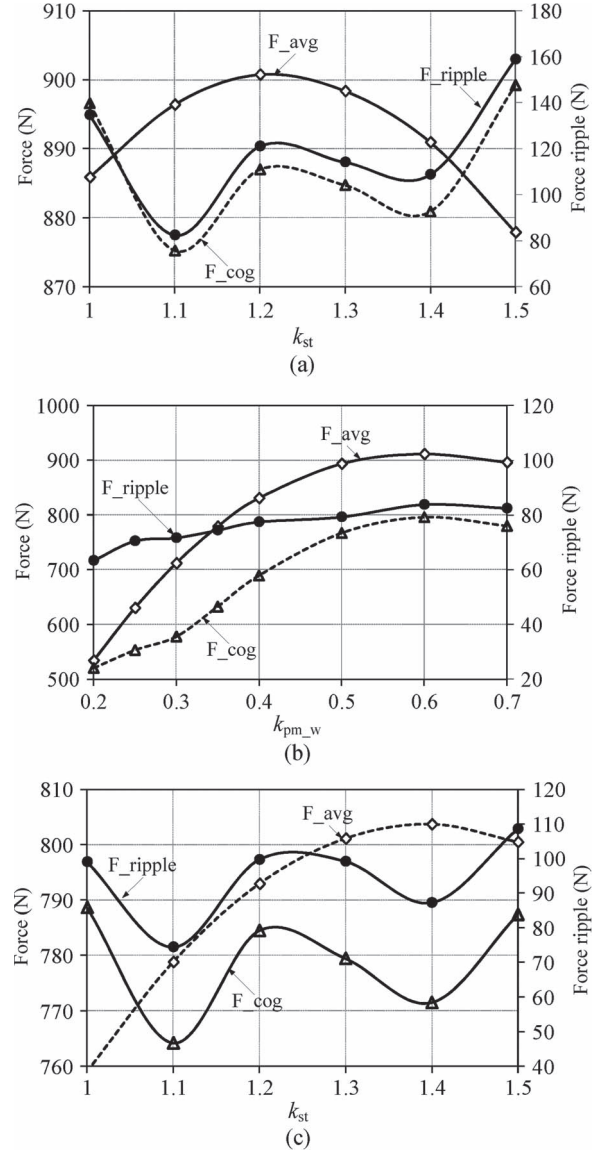


Fig. 11. Force performance of the conventional LFSPM motor versus different key parameters. (a) At different k_{st} values. (b) At different PM dimensions. (c) At different k_{st} values again.

utilization ratio, $k_{pm-w} = 0.35$ is adopted in the conventional motor.

- 3) Coefficient k_{st} is optimized again when $k_{pm-w} = 0.35$. Fig. 11(c) shows the F_{avg} , F_{cog} , and F_{ripple} waveforms of the conventional motor versus k_{st} . Obviously, F_{cog} and F_{ripple} also reach the minimum value at $k_{st} = 1.1$, while F_{avg} is about 97% of the maximum value at $k_{st} = 1.4$. Hence, considering the PM utilization ratio and force ripple, $k_{st} = 1.1$ and $k_{pm-w} = 0.35$ are adopted in the conventional LFSPM motor for comparison with the CMLFSPM motor.

The detailed key dimensions and electromagnetic performance are listed in Table VI. It can be seen that the back EMF, F_{avg} , F_{cog} , F_{ripple} , and mover iron volume of the CMLFSPM motor are about 102%, 98%, 61.8%, 68.8%, and 81.8% of the optimized conventional motor, respectively. Hence, it should be mentioned that the CMLFSPM motor does

TABLE VI
COMPARISON OF PERFORMANCES OF BOTH MOTORS

Items	CMLFSPM	Conventional
w_{pm} (mm)	$0.7 \cdot \tau_m / 4$	$0.35 \cdot \tau_m / 4$
w_{st} (mm)	$1.1 \cdot \tau_m / 4$	$1.1 \cdot \tau_m / 4$
EMF (V)	61.67	60.43
F_{avg} (N)	763.21	778.82
F_{cog} (N)	28.83	46.66
F_{ripple} (N)	51.25	74.43
Mover iron volume (cm ³)	1929.312	2356.673
Stator	Same	Same
PM volume	Same	Same
Armature mass	Same	Same

not offer better magnet utilization (F_{avg}/PM volume) than the conventional LFSPM motor when they have the same total PM volume. However, it has a much smaller cogging force, smaller thrust force ripple, and less material for the mover iron.

IV. ELECTROMAGNETIC PERFORMANCE

In this section, the electromagnetic performances of the CMLFSPM motor, including the back EMF and its harmonics, cogging force, and normal force, are calculated using FEM and are compared with those of the conventional LFSPM.

A. Back EMF

Fig. 12 depicts the back EMF waveforms and its harmonics induced in coil A1, coil A2, and phase A at the rated speed. It can be seen that the back EMF in coil A1 is complementary with the one in coil A2. Also, their maximum and minimum values are nearly the same. Because the even harmonics in the phase back EMF are significantly reduced, the back EMF is also sinusoidal, and its THD is only 2.79%. For the conventional LFSPM motor shown in Fig. 2(a), the relative positions with the stator of end coil A1 and middle coil A3 are the same. Fig. 13 shows the back EMF induced in end coil A1 and middle coil A3 of the conventional LFSPM motor. It can be seen that the back EMF in end coil A1 is smaller than the one in coil A3, which is caused not only by the end effect but also by the asymmetry of magnetic circuit in both coils as shown in Fig. 2(b) and (c). However, the back EMF waveforms in middle coil A2 and coil A4 are nearly the same.

B. Thrust Force and Cogging Force

The cogging force and normal force are calculated by means of FEM through two steps. First, the cogging forces of the three-phase models are calculated separately. Fig. 14(a) shows the cogging force waveforms when the mover only consists of one-phase model, namely, phase A, phase B, or phase C model, in which F_{x_AA} , F_{x_BB} , F_{x_CC} , and F_x denotes the cogging forces of phase A, phase B, and phase C, and the sum of the three-phase cogging forces, respectively. It can be seen that F_{x_AA} is very close to sinusoidal waveform with 180° period and $F_{x_AA} = 0$ at the positions: 0°, 90°, 180°, and 270°. As can be seen from Fig. 3, phase A consists of two “E”-shaped modules with 180° shift. At positions 0°, 90°, 180°, and 270°, the central axes of the left “E”-shaped module, right “E”-shaped

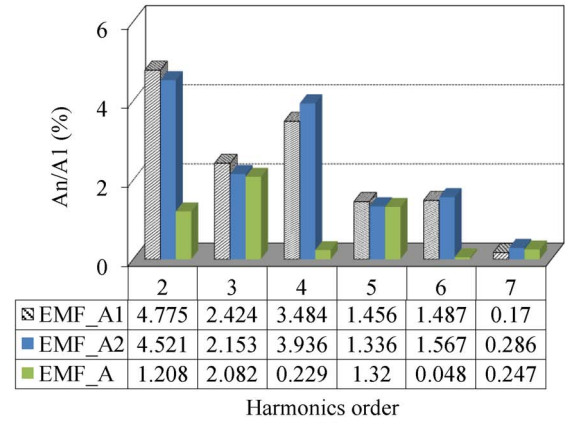
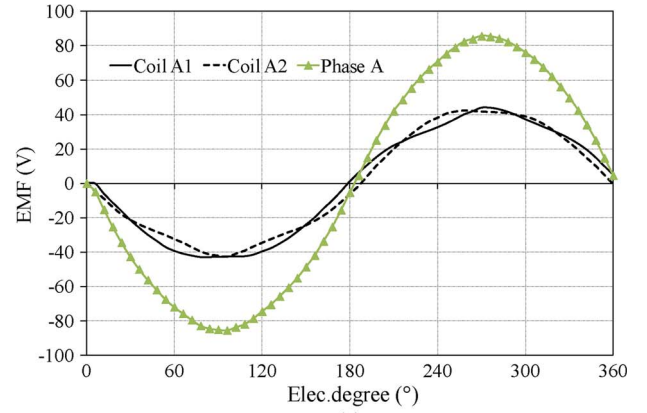


Fig. 12. Back EMF and its harmonics of the CMLFSPM motor. (a) Back EMF. (b) Harmonics distribution.

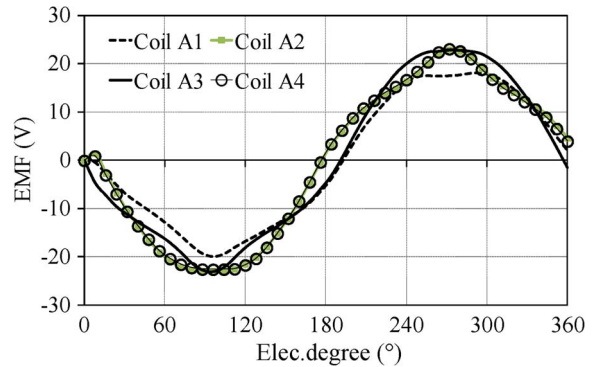


Fig. 13. Back EMF waveforms of the conventional LFSPM motor in end coil and middle coils of phase A.

module, and two “E”-shaped modules align with the central axis of the stator tooth and slot. Hence, $F_{x_AA} = 0$ at those balance positions. Also, the relative displacement between two adjacent phases is 120°; $F_{x_BB} = 0$ at the balance positions of 30°, 120°, 210°, and 300°; and $F_{x_CC} = 0$ at the balance positions of 60°, 150°, 240°, and 330°. The sum value of the fundamental components of the three-phase modules is equal to zero. Hence, the total cogging force of the proposed motor is very small. Similarly, it can be seen from Fig. 14(b) that the ripples of the normal force of phase A, phase B, and phase C are big, but the ripple of the average value of three phases F_{y_avg} is very small.

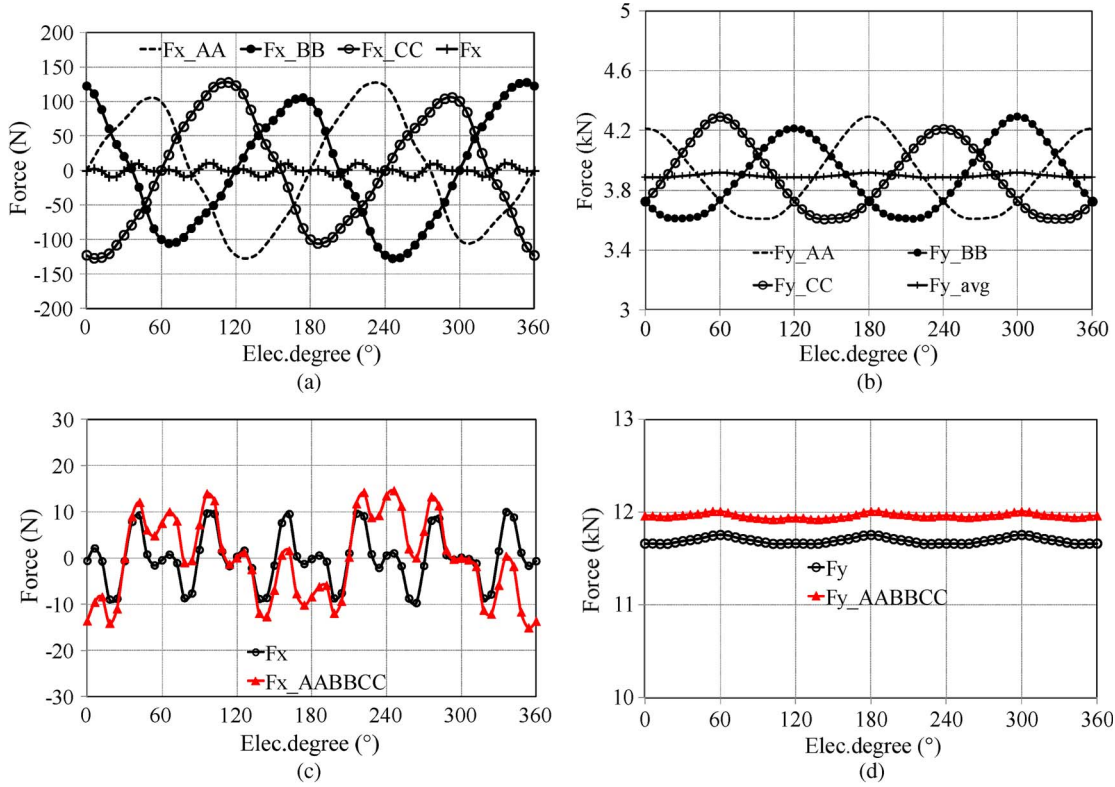


Fig. 14. Cogging force and normal force waveforms of the CMLFSPM motor. (a) Cogging force of each module and its sum value. (b) Normal force of each module and its average value. (c) Cogging force based on two methods. (d) Normal force based on two methods.

It should be noted that the end effects in the aforementioned analysis are not the same as the actual one. In this section, the total cogging force and normal force are calculated directly using FEM and are compared with the first method. It can be seen from Fig. 3 that the end effects of the left sides of phase A and phase C are not the same as the one on the right side. Because phase B is at the middle of the proposed motor, the total cogging forces calculated by the two methods should have the same balance positions with phase B, i.e., the total cogging force is equal to zero at the balance positions of 30°, 120°, 210°, and 300°. Fig. 14(c) shows the total cogging force of the proposed motor calculated directly by FEM F_{x_AABBCC} and the sum value of each phase model F_x . It can be seen that F_{x_AABBCC} matches well with F_x around the balance positions, while F_{x_AABBCC} is bigger than F_x in ranges of 30°–120° and 210°–300° and smaller than F_x in ranges of 0°–30°, 120°–210°, and 300°–360° due to the unbalanced left and right end effects. However, the shape and peak value of the cogging force of both methods are similar. The shape and peak value of the normal forces of both methods F_y and F_{y_AABBCC} are also similar as shown in Fig. 14(d).

V. EXPERIMENTAL RESULTS

To validate the associated FEM results of the CMLFSPM motor, a three-phase CMLFSPM prototype based on the optimized dimensions has been built. It should be mentioned that the PM width and mover yoke height of the prototype motor are integer values ($w_{pm} = 7$ mm and $h_{my} = 14$ mm). Therefore, there is a little error between the prototype motor and

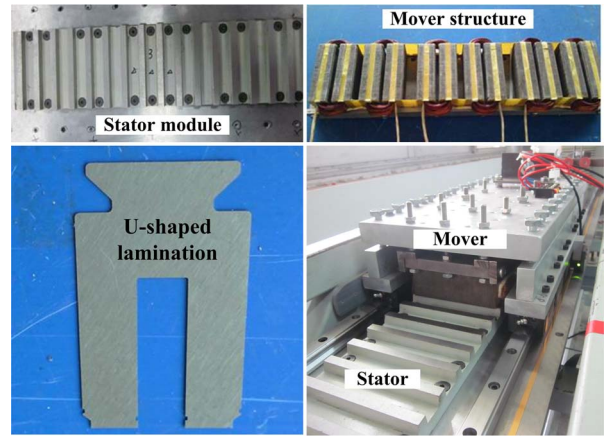


Fig. 15. Prototype of the CMLFSPM.

the optimized motor ($w_{pm} = 7.35$ mm and $h_{my} = 13.65$ mm). The detailed structure, including the mover, the stator, the “U”-shaped laminated segments, and the prototype motor, is shown in Fig. 15. The simulated and measured open-circuit back EMF values of the prototype motor at a speed of 1.05 m/s are compared in Fig. 16. It can be seen that the simulated results exhibit a good agreement with the experimental ones. The discrepancies between the experimental and simulation results are about 10%, which we believe are mainly caused by the end effects as in the stator PM machines [20], manufacturing imperfection, and measurement error.

Fig. 17(a) shows the experiment test bed of the cogging force. The mover is connected with suitable weights through a force sensor and a steel wire rope. When the weight pulls the mover

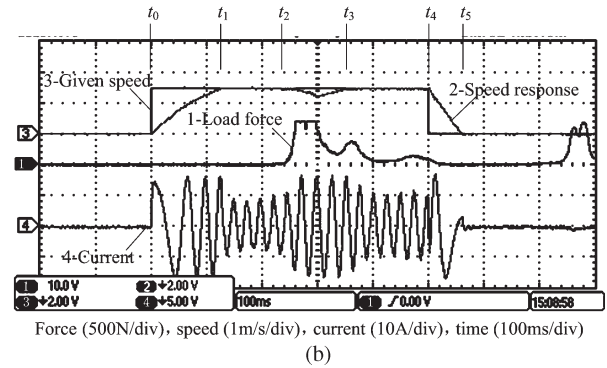
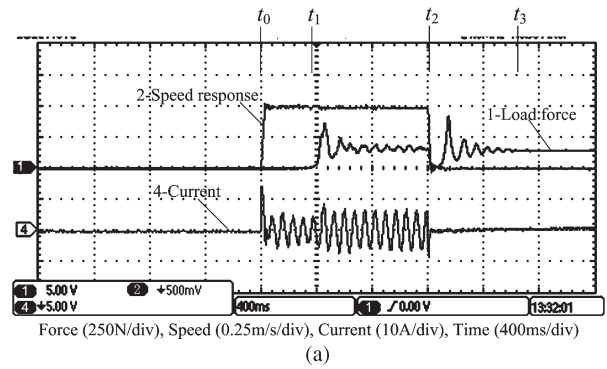
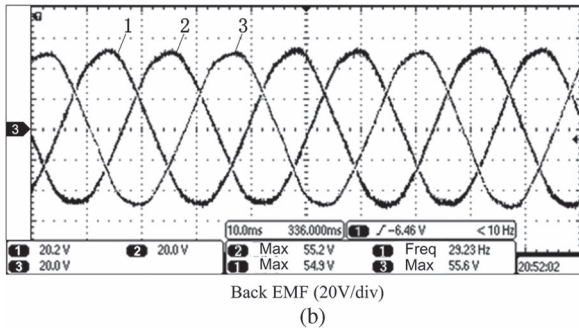
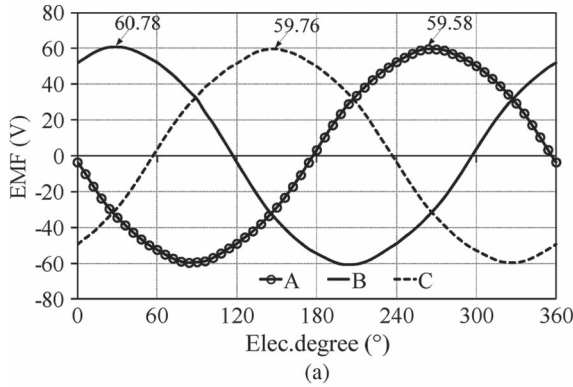


Fig. 16. Back EMF waveforms at 1.05 m/s. (a) FEM results. (b) Experimental results.

Fig. 18. Measured waveforms of speed, current, and force at different given speeds and sudden load (15.2 kg). (a) Given speed is equal to 0.5 m/s. (b) Given speed is equal to 1.5 m/s.

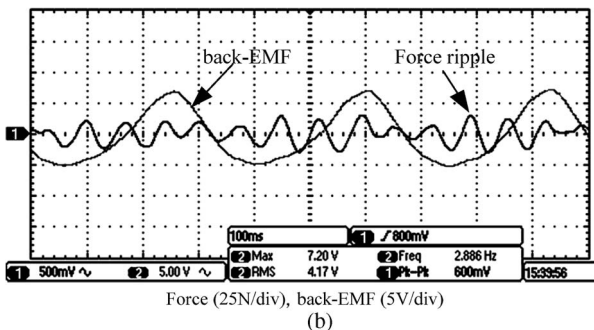
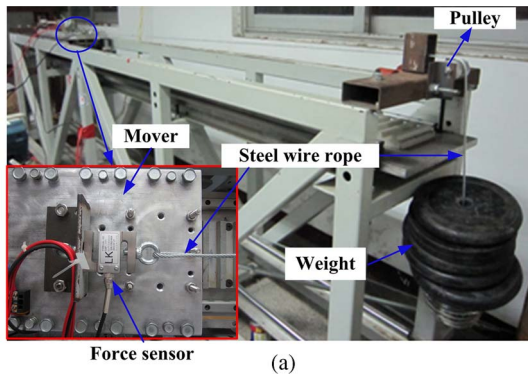


Fig. 17. Test bed and experimental results of the cogging force. (a) Test bed for the cogging force. (b) Experimental results of the cogging force and phase back EMF.

running at a slow speed, the waveforms of the phase back EMF and force ripple can be tested as shown in Fig. 17(b). It can be seen that the measured cogging force peak-to-peak value is about 30 N. The cogging force peak-to-peak value based on FEM is 28.83 N (Table VI). There is an error of 1.17 N between

the FEM and measured results. This is because the measured force ripple includes not only the cogging force but also the friction force ripple caused by normal force, pulley, and linear guide. Therefore, the FEM results of the cogging force are acceptable. Due to the influence of the cogging force, the mover speed is not constant in this process. Hence, the measured phase back EMF in Fig. 17(b) is not symmetrical.

To validate the dynamic performance of the proposed CMLF-SPM motor, the speed control response of the proposed motor at different given speeds based on current vector control method ($I_d = 0$) has been tested as shown in Fig. 18.

Fig. 18(a) shows the responses of speed, current, and load force when the given speed is 0.5 m/s. It can be seen that the mover start time is about 20 ms. At time t_1 , a sudden weight (15.2 kg) was connected with the mover through the force sensor and steel wire rope. It can be seen that the mover speed is kept constant at 0.5 m/s and the value of the force sensor changes around 148 N due to the inertia of the weight. At time t_2 , the given speed becomes zero, and the mover speed reduces to zero after 20 ms. Because the weight continues to move up due to inertia, the value of the force sensor is equal to zero. After the weight stops and then free falls, the value of the force sensor has a great fluctuation and then stops at 148 N until time t_3 . However, the speed is always kept at the given speed (0 m/s).

Fig. 18(b) shows the responses of speed, current, and load force when the given speed is at 1.5 m/s. It can be seen that the start time is about 125 ms. At time t_2 , a sudden weight (15.2 kg) was connected with the mover through the force sensor and steel wire rope. It can be seen the mover speed has some fluctuation and then stabilizes at 1.5 m/s at t_3 . Between t_2

and t_3 , because the value of the force sensor reaches the limit value (700 N), the force waveform is flat. Because the inertia of the weight is too big at 1.5 m/s, the value of the force sensor is not constant. At time t_4 , the given speed is equal to zero, and the mover speed reduces to zero at t_5 after 60 ms. However, the weight will continue to move up due to inertia, so the value of the force sensor is equal to zero. After the weight stops and free falls, the value of the force sensor has a great fluctuation, but the speed is always kept at the given speed (0 m/s).

It should be mentioned that the friction force is big especially at a high speed. This friction force can be reduced by using a high-quality linear guide.

VI. CONCLUSION

In this paper, the structure and performance of a new modular LFSPM motor have been analyzed and optimized by means of FEM. Then, the influences of some key parameters on the electromagnetic performance of the proposed motor have been investigated. Also, the conventional LFSPM has been optimized and compared with the proposed motor. Furthermore, the open-circuit back EMF, normal force, and cogging force of the proposed motor have been analyzed based on the optimal dimensions. To verify the simulation results of the CMLFSPM motor, a prototype motor has been built and tested. The experimental results agree well with the predicted results from the mathematics model and FEM. Moreover, the dynamic performances of speed closed-loop control of the LFSPM motor have been investigated for the first time. The merits of the proposed motor are summarized as follows.

- 1) The CMLFSPM incorporates the simple stator of LSR motors and the high power density of LPMS motors, which is very suitable for long stator applications to reduce system cost.
- 2) Different from the conventional LFSPM motor, the CMLFSPM motor has a complementary mover structure, offering symmetrical, balanced, and sinusoidal back EMF, smaller cogging force, and smaller thrust force ripple.
- 3) Different from the conventional LFSPM motor, the CMLFSPM motor has independent three-phase armature windings and a smaller mutual inductance, thus providing a high fault-tolerant ability.
- 4) Different from the conventional LFSPM motor, the CMLFSPM motor has modular mover and stator, which is easy to assemble. Also, it can be a component of a multimachine system.

REFERENCES

- [1] J. F. Gieras and Z. J. Piech, *Linear Synchronous Motors: Transportation and Automation Systems*. Boca Raton, FL, USA: CRC, 2000.
- [2] T. Higuchi and S. Nonaka, "On the design of high efficiency linear induction motors for linear metro," *Elect. Eng. Jpn.*, vol. 137, no. 2, pp. 36–43, Nov. 2001.
- [3] S. Yoon, J. Hur, and D. Hyun, "A method of optimal design of single-sided linear induction motor for transit," *IEEE Trans. Magn.*, vol. 33, no. 5, pp. 4215–4217, Sep. 1997.
- [4] G. Stumberger, D. Zarko, M. T. Aydemir, and T. A. Lipo, "Design and comparison of linear synchronous motor and linear induction motor for

electromagnetic aircraft launch system," in *Proc. IEMDC*, Jun. 2003, pp. 494–500.

- [5] S. W. Zhao, N. C. Cheung, W. C. Gan, J. M. Yang, and J. F. Pan, "A self-tuning regulator for the high-precision position control of a linear switched reluctance motor," *IEEE Trans. Ind. Electron.*, vol. 54, no. 5, pp. 2425–2434, Oct. 2007.
- [6] K. T. Chau, C. C. Chan, and C. Liu, "Overview of permanent-magnet brushless drives for electric and hybrid electric vehicles," *IEEE Trans. Ind. Electron.*, vol. 55, no. 6, pp. 2246–2257, Jun. 2008.
- [7] R. Cao, M. Cheng, C. Mi, W. Hua, and W. Zhao, "A linear doubly salient permanent magnet motor with modular and complementary structure," *IEEE Trans. Magn.*, vol. 47, no. 12, pp. 4809–4821, Dec. 2011.
- [8] Z. Q. Zhu, X. Chen, and J. Chen, "Novel linear flux switching permanent magnet machines," in *Proc. ICEMS*, Oct. 2008, pp. 2948–2953.
- [9] M. Jin, C. Wang, and J. Shen, "A modular permanent magnet flux-switching linear machine with fault tolerant capability," *IEEE Trans. Magn.*, vol. 45, no. 8, pp. 3179–3186, Aug. 2009.
- [10] S.-U. Chung, H.-J. Lee, and S.-M. Hwang, "A novel design of linear synchronous motor using FRM topology," *IEEE Trans. Magn.*, vol. 44, no. 6, pp. 1514–1517, Jun. 2008.
- [11] M. Cheng, W. Hua, J. Zhang, and W. Zhao, "Overview of stator-permanent magnet brushless machines," *IEEE Trans. Ind. Electron.*, vol. 85, no. 11, pp. 5087–5101, Nov. 2011.
- [12] J. Zhang, M. Cheng, Z. Chen, and W. Hua, "Comparison of stator-mounted permanent-magnet machines based on a general power equation," *IEEE Trans. Energy Convers.*, vol. 24, no. 4, pp. 826–834, Dec. 2009.
- [13] W. Zhao, M. Cheng, W. Hua, H. Jia, and R. Cao, "Back-EMF harmonic analysis and fault-tolerant control of flux-switching permanent-magnet machine with redundancy," *IEEE Trans. Ind. Electron.*, vol. 58, no. 5, pp. 1926–1935, May 2011.
- [14] J. T. Chen and Z. Q. Zhu, "Comparison of all- and alternate-poles-wound flux-switching PM machines having different stator and rotor pole numbers," *IEEE Trans. Ind. Appl.*, vol. 46, no. 4, pp. 1406–1415, Jul./Aug. 2010.
- [15] R. Cao, M. Cheng, C. Mi, W. Hua, X. Wang, and W. Zhao, "Modeling of a complementary and modular linear flux-switching permanent magnet motor for urban rail transit applications," *IEEE Trans. Energy Convers.*, vol. 27, no. 2, pp. 489–497, Jun. 2012.
- [16] R. Cao, M. Cheng, and W. Hua, "Investigation and general design principle of a new series of complementary and modular linear FSPM motors," *IEEE Trans. Ind. Electron.*, vol. 6012, pp. 5436–5446, Dec. 2013.
- [17] W. Hua, M. Cheng, Z. Q. Zhu, and D. Howe, "Analysis and optimization of back-EMF waveform of a flux-switching permanent magnet motor," *IEEE Trans. Energy Convers.*, vol. 23, no. 3, pp. 727–733, Sep. 2008.
- [18] J. Wang, D. Howe, and Z. Lin, "Design optimization of short-stroke single-phase tubular permanent magnet motor for refrigeration applications," *IEEE Trans. Ind. Electron.*, vol. 57, no. 1, pp. 327–334, Jan. 2011.
- [19] R. Cao, C. Mi, and M. Cheng, "Quantitative comparison of flux-switching permanent magnet motors with interior permanent magnet motor for EV, HEV, and PHEV applications," *IEEE Trans. Magn.*, vol. 48, no. 8, pp. 2374–2384, Aug. 2012.
- [20] Z. Q. Zhu, Y. Pang, W. Hua, M. Cheng, and D. Howe, "Investigation of end effect in permanent magnet brushless machines having magnets on the stator," *J. Appl. Phys.*, vol. 99, no. 8, pp. 08R319-1–08R319-3, Apr. 2006.



Ruiwu Cao (S'10) received the B.S. degree in electrical engineering from Yancheng Institute of Technology, Yancheng, China, in 2004 and the M.S. degree in electrical engineering from Southeast University, Nanjing, China, in 2007, where he has been working toward the Ph.D. degree in electrical engineering since 2009.

From August 2010 to November 2011, he was a joint Ph.D. student with the College of Electrical and Computer Science, University of Michigan, Dearborn, MI, USA, funded by China Scholarship Council. His areas of interests include design, analysis, and control of rotary and linear permanent-magnet machines.



Ming Cheng (M'01–SM'02) received the B.Sc. and M.Sc. degrees from the Department of Electrical Engineering, Southeast University, Nanjing, China, in 1982 and 1987, respectively, and the Ph.D. degree from the Department of Electrical and Electronic Engineering, The University of Hong Kong, Hong Kong, in 2001.

Since 1987, he has been with Southeast University, where he is currently a Professor with the School of Electrical Engineering and the Director of the Research Center for Wind Power Generation. His teaching and research interests include electrical machines, motor drives for electric vehicles, and renewable-energy generation. He is the author or coauthor of over 300 technical papers and four books and holds 45 patents in these areas.

Prof. Cheng is a Fellow of The Institution of Engineering and Technology. He has served as chair and organizing committee member for many international conferences.



Wei Hua (M'07) was born in Jiangsu, China, in 1978. He received the B.S. and Ph.D. degrees in electrical engineering from Southeast University, Nanjing, China, in 2001 and 2007, respectively.

He is currently with Southeast University, where he is a Professor and the Deputy Dean of the Department of Electrical Machines and Control. His areas of interest include design, analysis, and control of the novel permanent-magnet machines and switched reluctance machines. He is the author of more than 100 published papers on these topics.



Chunting Chris Mi (S'00–A'01–M'01–SM'03–F'12) received the B.S.E.E. and M.S.E.E. degrees in electrical engineering from Northwestern Polytechnical University, Xi'an, China, and the Ph.D. degree in electrical engineering from the University of Toronto, Toronto, ON, Canada.

He is a Professor of electrical and computer engineering and the Director of the newly established DOE-funded GATE Center for Electric Drive Transportation, University of Michigan, Dearborn, MI, USA. His research interests include electric drives,

power electronics, electric machines, renewable-energy systems, and electrical and hybrid vehicles. He has conducted extensive research and has published more than 100 articles. He is a Guest Editor of the *International Journal of Power Electronics*.

Dr. Mi is an Associate Editor of the IEEE TRANSACTIONS ON VEHICULAR TECHNOLOGY, IEEE TRANSACTIONS ON POWER ELECTRONICS, and IEEE POWER ELECTRONICS LETTERS; Associate Editor of the IEEE TRANSACTIONS ON INDUSTRY APPLICATIONS; and Senior Editor of the IEEE VEHICULAR TECHNOLOGY MAGAZINE.